

## **Electrochemical and Microstructural Analysis of a Modified Gas Diffusion Layer for a PEM Water Electrolyzer**

*J.C. Cruz<sup>1,\*</sup>, R. Barbosa<sup>2</sup>, B. Escobar<sup>3</sup>, Z. Zarhri<sup>4</sup>, D.L. Trejo- Arroyo<sup>4</sup>, B. Pamplona<sup>1,5</sup>, L. Gómez-Barba<sup>5</sup>*

<sup>1</sup> Tecnológico Nacional de México/I.T. Chetumal; Insurgentes 330, Chetumal 77013, QR, México.

<sup>2</sup> Universidad de Quintana Roo, Boulevard Bahía s/n, 77019, Chetumal, Q. Roo, México.

<sup>3</sup> CONACYT-Centro de Investigación Científica de Yucatán, Parque Científico y Tecnológico de Yucatán. Carretera Sierra Papacal–Chuburna Puerto, km 5. Sierra Papacal, C.P. 97302, Mérida, Yucatán.

<sup>4</sup> CONACYT-Tecnológico Nacional de México/I.T. Chetumal; Insurgentes 330, Chetumal 77013, QR, México.

<sup>5</sup> Departamento de Sistemas de Información, Universidad de Guadalajara, Zapopan, Jalisco, México, 45100.

\*E-mail: [jcruz@itchetumal.edu.mx](mailto:jcruz@itchetumal.edu.mx)

*Received:* 19 December 2019 / *Accepted:* 4 March 2020 / *Published:* 10 May 2020

Water electrolysis is an electrochemical process capable of producing high-purity hydrogen ( $H_2 \approx 100\%$ ). However, due to high anodic operating potentials, which are greater than 1.8 V in acidic media, they tend to degrade the components that are currently designed. One of the main components is the gas diffusion layer (GDL) of a proton exchange membrane water electrolyzer (PEMWE). A commonly used carbon GDL is coal. However, the acid medium increases the potential to 1.4 V, which causes the GDL to become oxidized and degrade; the above result is due to the generation of carbon products that poison the electrode and the blocking of active sites, all of which decrease the performance of the cell. In this work, the results of a morphological study on a modified titanium porous matrix are presented. The analysis includes the determination of the microstructural influence on mass transport through numerical simulation and statistical electrochemical characterization techniques. Two different microstructural attacks are performed to modify the porous matrix. These attacks consist of an acidic mixture of 17 and 27% v/v HCl/H<sub>2</sub>SO<sub>4</sub> and an attack by a 0.1 M oxalic acid solution; these attacks were performed at different times. Afterward, the GDLs were characterized by scanning electron microscopy (SEM) at different magnifications to determine significant microstructural differences between the three matrices (the two that are modified and the one without modification) and their stochastic reconstruction. Subsequently, a surface area characterization is performed by the BET absorption technique to calculate the porosity of the different matrices.

**Keywords:** Water Electrolysis; Microstructural Analysis; Gas Diffusion Layer; Porous Matrix; Microstructural Attack.

## 1. INTRODUCTION

In 2030, the world population is estimated by the United Nations to reach 8.5 billion; this accelerated growth will demand sustainable energy generation through alternative green sources [1–3]. Within such scenarios, hydrogen fuel is a low-carbon option to satisfy future requirements as an energy source [4]. On the other hand, proton exchange membrane fuel cells (PEMFCs) and water electrolyzers (PEMWEs) are topics of scientific investigation due to their high efficiency and potential use in diverse scenarios or applications [5–8]. Both are good prospective technologies for the production and utilization of hydrogen as an energy carrier [7,9–12].

Many research efforts have been conducted to improve the electrocatalysis process for the oxygen electrode of [13–19]fuel cells (FCs). However, the use of a gas diffusion layer can decrease the performance and reliability of the catalytic layer (CL) on the oxygen electrode side. The properties of titanium and carbon paper have been shown to support mass transport as bifunctional oxygen electrode materials [20–22]. During water electrolysis, titanium will be degraded by oxidation, thus generating low conductivity. Likewise, the fuel cell performance will decrease due to carbon paper corrosion by the active oxygen species at a high operating potential [13,23–25].

The reactant gases enter a PEMFC through the etched channel to arrive between the gas diffusion layer and the catalyst layer, where they undergo electrochemical reactions. The catalyst works as a support to accelerate the chemical transformation rate inside the cell; the electrons are collected and flow due to the electrical conductivity of the carbon, while the produced hydrogen protons pass through the membrane [26,27]. According to diverse micrometer samples of the catalyst layer, different theories have been formulated; these theories are composed of agglomerates in a porous matrix [28,29]. The agglomerates are defined as small spheres covered with a fine layer of ionomer and Pt/C particles on the inside [4,13,30]. Therefore, the CL is considered a random heterogeneous material. Thus, this characteristic establishes various phases that are integrated in the catalyst due to the particular properties that differentiate them (i.e., voids, other solid material, gases, or liquids).

Proportionality coefficients for mass, energy and charge transport in a heterogeneous material are significantly affected by the properties of the various phases from which the catalyst is composed; the properties may be affected by the volume fraction composition or by the structure of such phases. For this reason, an effective transport coefficient (ETC) is defined for a heterogeneous material as a proportionality coefficient, which characterizes the domain of the material [4,31]. Nevertheless, these studies have only investigated CLs, not GDLs. This paper presents the microstructural statistical analysis differences between the diffusion layer matrix (modified and without surface modification) and its stochastic reconstruction. In addition, a comparative analysis of the areas modified by simulation and electrochemical processes is developed to produce a microscale morphology for anchoring protective nanoparticles.

## 2. EXPERIMENTAL

### 2.1 Pretreatment of the Ti substrates

The Ti samples were ultrasonically cleaned in ethanol and distilled water and then immersed in a 0.1 M oxalic acid ( $C_2H_2O_4$ ) solution at 60 °C for 5 h. After the treatment, the porous matrix was cleaned in hot distilled water and dried at room temperature [32–35].

### 2.2 Physicochemical characterization of Ti

The morphology was investigated using a Vega Tescan SEM microscope operated at 200 kV. Samples were studied by SEM at different resolutions. The following micrometric scales were empirically selected: superficial scale at a 100x resolution and a micropore scale at a 2000x resolution. Additionally, an energy dispersive spectroscopy (EDS) analysis was carried out with an SEM microscope at 1000x. Subsequently, a surface area characterization was performed by the BET absorption technique with equipment from Quantachrome Instruments to calculate the porosity of the different matrices. X-ray diffraction (XRD) was performed with a Bruker D8 Advance diffractometer, and was operated at  $0.03^\circ \text{ min}^{-1}$ .

### 2.3 Electrochemical characterization of Ti

The electrochemical behavior of the Ti porous matrix was evaluated by cyclic voltammetry, anodic polarization curves, linear voltammetry and electrochemical impedance spectroscopy from 10 kHz to 0.1 Hz. The electrochemical characterization was performed in a PGSTAT Autolab 302 potentiostat/galvanostat equipped with a booster of 20 A (Metrohm®) and a frequency response analyzer (FRA). Cyclic voltammetry curves were obtained using a conventional three-electrode cell with a 0.5 M  $H_2SO_4$  solution in a range of potentials from -0.3 to 1.3 V at a  $100 \text{ mV s}^{-1}$  scan rate. The working electrode was a porous Ti sample. A Hg/Hg<sub>2</sub>SO<sub>4</sub> electrode was used as the reference electrode, and a Pt rod was used as the counter electrode. The electrochemical area was determined in a 0.1 M KCl solution at room temperature by cyclic voltammetry following the investigations of Trasatti and coworkers [36] for the analysis of the corrosion process using polarization curves from the open circuit potential to 1.8, 2 and 2.2 V; the above method simulates the water electrolysis process in a conventional electrolyzer.

### 2.4 Structural reconstruction algorithm

The reconstruction of the microstructure by a simulated annealing (SA) method was implemented for a numerical analysis of the change in microstructure. This methodology includes the following steps: (1) binarization of an image; 2) stochastic reconstruction by SA; and (3) statistical characterization of the change in microstructure. These numerical results included the surface fraction change and the two-point correlation function ( $S_j$ ) of an assembly composed of W and realizations  $\omega$ .

The gas diffusion layer can be defined as a randomly distributed heterogeneous material (RHM). The SA method [4,31,33,34] can be applied to reconstruct our GDL with and without treatment and compare the superficial change. SA is based on a well-known physical fact: if the system is heated to high temperatures (T) and then gently cooled to absolute zero, the system will balance to its original state. The SA method has been detailed in the literature. However, it is essential to define the mathematical basis of space and the statistical descriptors.

The statistical analysis considers the assembly ( $\Omega$ ) of a different random seed and the mean of the realizations ( $\omega$ ). Each realization  $\omega$  represents the domain  $v$  of the system (or material) studied, which is fractionated into nodes of phase  $j$ . We can define the region in space  $v_j(\omega)$ , its respective surface fraction  $\Phi_j(\omega)$ , and the index function ( $I_j(x)$ ):

$$I_j(x) = \begin{pmatrix} 1, & \text{if } x \in v_j(\omega), \\ 0, & \text{otherwise,} \end{pmatrix} \tag{1}$$

In this digital system definition, a two-point correlation function ( $S_j$ ) and the linear path correlation function ( $P_j$ ) can be easily defined by equations 2a and 2b:

$$S_j = \langle I_j(x) I_j(x+r) \rangle \tag{2a}$$

$$P_j = \int I_j(x + \alpha r) d\alpha \tag{2b}$$

where the angle bracket is for the average of the expectation of the  $I_j(x)$  function,  $x$  is any position in  $v_j(\omega)$ ,  $r$  is a vector of the relative position with a selected magnitude and direction and  $\alpha$  is the segment evaluation.

For the SA reconstruction, the two functions are considered in both studied phases ( $j_1$  and  $j_2$ ), and equation (3) defines the error (or "energy") between the reference system and the "current" system ( $E_{SA}$ ):

$$E_{SA} = \sum_r (F'(r) - F(r))^2 \tag{3}$$

$$\text{where } F(r) = \frac{1}{4} (\sum S_{j_1}(r) + \sum S_{j_2}(r) + \sum P_{j_1}(r) + \sum P_{j_2}(r)) \tag{3a}$$

$F(r)$  characterizes the reference system, and  $F'(r)$  characterizes the "current" system. A reduction in  $E_{SA}$  is achieved by the exchange of the phase of two randomly selected pixels ( $\Phi_j(\omega) = \text{constant}$ ) and the calculations of the new system energy ( $E'_{SA}$ ) and the energy difference  $\Delta E_{SA} = E'_{SA} - E_{SA}$ . The phase change of a pixel is accepted if the probability  $P(\Delta E_{SA})$  is met:

$$P(\Delta E_{SA}) = \begin{pmatrix} 1, & \Delta E_{SA} \leq 0, \\ \exp\left(\frac{-\Delta E_{SA}}{T}\right), & \Delta E_{SA} > 0, \end{pmatrix} \tag{4}$$

The cooling or "annealing calendar", which governs the value and the exchange rate  $T$ , is chosen to be slow enough to allow the system to converge to the desired state ( $F(r)$ ), while being fast enough to avoid being trapped in states of minimum energy:-

In the results and discussion section, the surface fraction  $\Phi_j(\omega)$  and  $S_j$  statistical descriptor show the change in microstructure due to the microstructural attack.

### 3. RESULTS AND DISCUSSION

#### 3.1. Microstructural analysis

Figure 1 shows the SEM photographs of the blank Ti sample, obtaining a different pore size and no homogenous distribution through the matrix. A smooth morphology was observed in the nonhomogeneous matrix particles. Figure 2 shows a Ti sample after 5 h of treatment, and the sample demonstrates a different surface morphology. A scale-like morphology with a high roughness suggests better adsorption for new materials at active sites. Small particles with no homogenous distribution can be observed, and a large surface area is assumed because of etching [33–36].

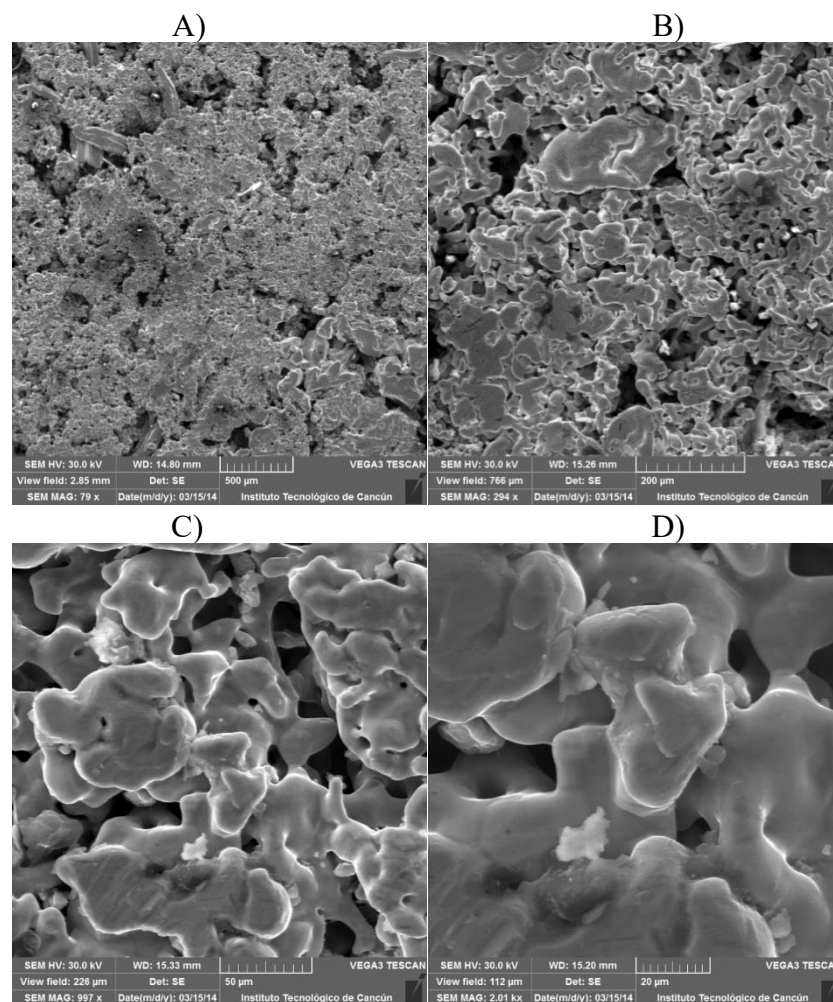


**Figure 1.** SEM images of Ti (blank) without an etching attack at different magnifications: a) 100x, b) 500x, c) 1000x, and d) 2000x.

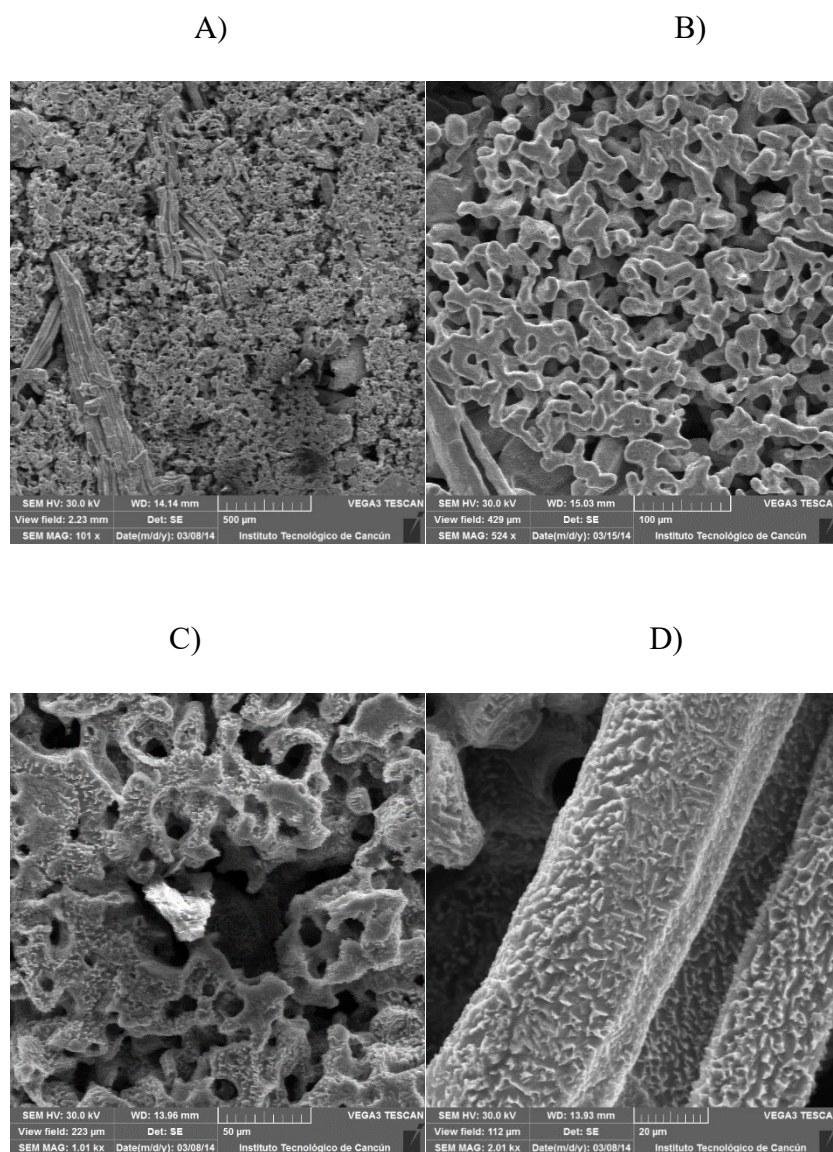
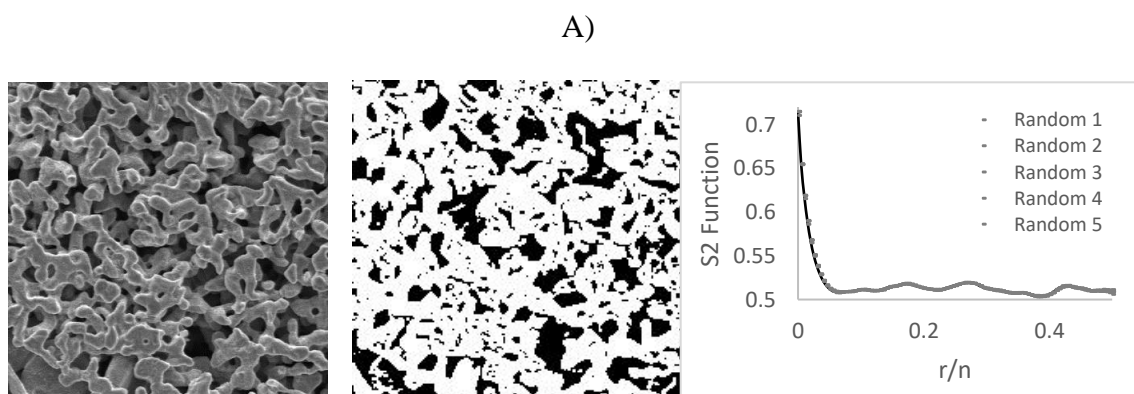


**Figure 2.** SEM images of Ti after an acid treatment ( $C_2H_2O_4$ ) at different magnifications: a) 100x, b) 500x, c) 1000x, and d) 2000x.



B)

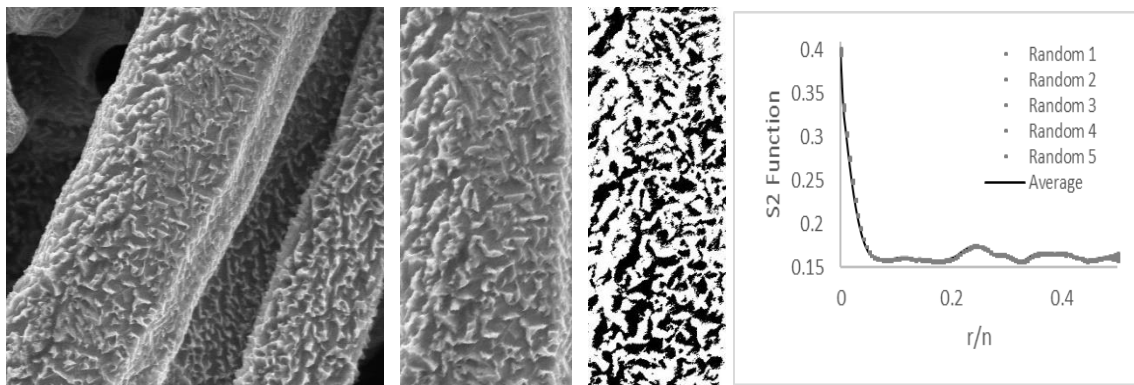


**Figure 3.** Analysis of the stochastic 2D-reconstruction of the samples without treatment (A) and with treatment (B).

According to the stochastic method surface analysis (Figure 3), an average of 5 random samples was calculated. The surface fraction of the unmodified solid is determined (Figure 3 A) as  $71.4\% \pm 0.001$  and the surface fraction of the pores is  $29\% \pm 0.001$ . The above results lead to a solid surface area calculation of  $94398.02 \pm 128.81 \mu\text{m}^2$  and an interface surface of  $5321.45 \pm 36.5 \mu\text{m}^2$ . In the same way, a modified fraction of  $39.9\% \pm 0.0013$  and a solid surface area of  $330.7 \pm 1.12 \mu\text{m}^2$  are obtained through reconstruction. An increase of  $39.9\% \pm 0.0013$  corresponding to  $3766480.86 \mu\text{m}^2$  can be determined.

Tables 1 and 2 present the elemental analysis on the surface, observing a decrease in some components, such as Si and Ca, as well as a large decrease in carbon. These elements can promote impurities or defects on the porous matrix, causing different responses in the diffusion and distribution of reactants; even the rate of corrosion of the carbon is affected. Cleaning the Ti sample demonstrates a more “pure” behavior and response, showing high corrosion resistance, good mechanical strength, and ions that are not too poisonous for the catalysts and membranes [32,34–38].

**Table 1.** EDS results of Ti (blank).

Element	[wt.%]	[norm. wt.%]	[norm. at.%]
Carbon	25.90132	20.21134	50.06139
Titanium	100.3304	78.28991	48.64504
Silicon	0.731969	0.571171	0.605021
Calcium	1.188716	0.92758	0.688545

**Table 2.** EDS results of Ti after the acid treatment.

Element	[wt.%]	[norm. wt.%]	[norm. at.%]
Titanium	133.1906	91.81537	73.78157
Carbon	11.87291	8.184631	26.21843

However, the metal can also show gradual surface corrosion in a highly acidic environment during electrolysis operation. The corrosion finally causes the formation of a passive oxide layer on the surface of the metal during electrolysis and fuel cell operation [35–38]. Investigating this material will improve its behavior and resistance to corrosion, while also acting as a good reactant distribution layer for the process mentioned above.

### 3.2. Crystal structure

XRD was used to investigate the changes in the phase structure of the titanium matrix. Figure 3 shows the effects of the acidic treatment with a  $C_2H_2O_4$  solution. It can be seen that with the acidic and temperature treatment, the peak intensity at  $2\theta = 38.4^\circ$  increases and the width of the (0 0 2) plane diffraction pattern of titanium becomes narrower. Similarly, the peaks at  $2\theta = 77.3^\circ$  and  $2\theta = 82.3^\circ$  of the (1 1 2) and (0 0 4) plane diffraction patterns, respectively, are increased and narrower but are also better defined after the treatment. Nevertheless, the peaks of the (1 0 0), (1 1 0) and (1 0 3) planes at  $2\theta = 53.0^\circ$ ,  $62.9^\circ$  and  $70.6^\circ$ , respectively, decrease but retain a well-defined arrow shape.

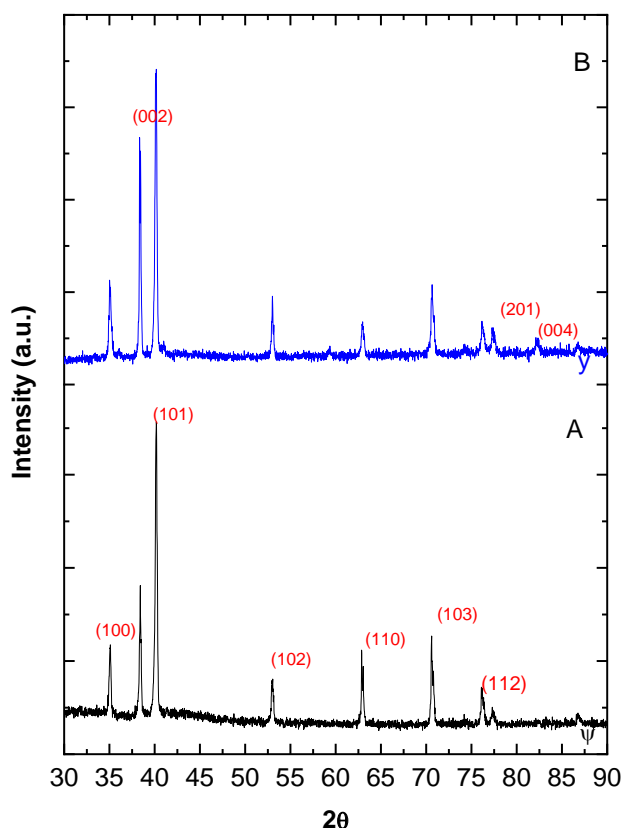


**Figure 3.** X-ray diffraction patterns of the matrix samples: a) Ti (blank) and b) Ti after the acid treatment with a  $C_2H_2O_4$  solution at 60 °C for 5 h.

### 3.3. BET surface area and pore structure

Figure 4 shows the pore size distribution curve calculated from the desorption branch of the nitrogen isotherm by the BJH method and the corresponding pore volume curve of the titanium matrix: A) blank and B) modified with a solution of  $C_2H_2O_4$  at  $60\text{ }^\circ\text{C}$  for 5 h. The pore size distribution calculated from the desorption branch of the nitrogen isotherm by the BJH (Barret-Joyner-Halenda) method shows a pair of narrow ranges of 20.0-40.0 nm with an average pore radius of 16.97 nm for the blank Ti sample. In contrast, for the Ti sample modified with a  $C_2H_2O_4$  solution, the figure shows a noticeably narrow range of 20.0-40.0 nm but with an average pore radius of 15.24 nm according to the BJH method. The abovementioned pore sizes (mesopores) suggest a rapid diffusion of various gaseous reactants and products during the electrolysis reaction and enhances the rate of distribution of reactants, thus avoiding a flood into the catalytic layer.

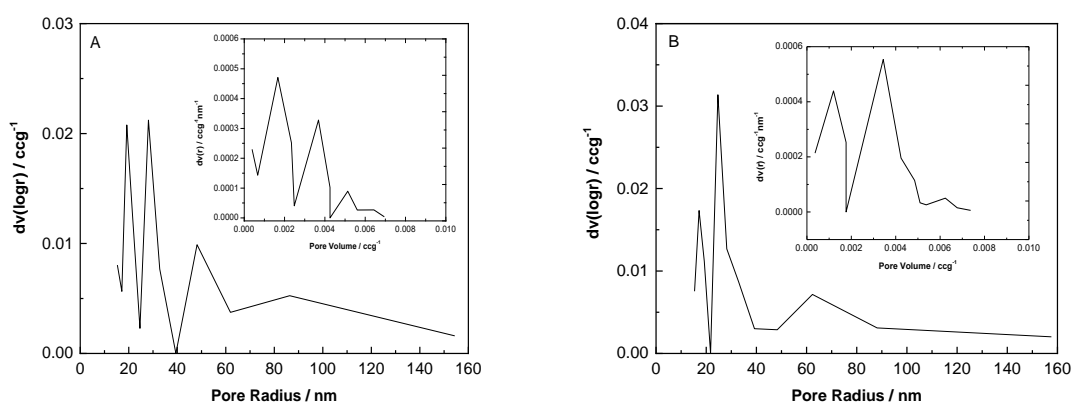


**Figure 4.** Pore size distribution curve calculated from the desorption branch of the nitrogen isotherm by the BJH method and the corresponding pore volume distribution of the A) porous Ti blank and B) porous Ti modified with a  $C_2H_2O_4$  solution at  $60\text{ }^\circ\text{C}$  for 5 h.

Table 3 shows a face-to-face comparison of different techniques: physicochemical, electrochemical and stochastic methods. The surface area (BJH) method evaluated the pore size and pore volume values and distribution; both of the titanium samples were similar with values of  $4.7 \pm 1.42$  and  $5.0 \pm 1.56\text{ m}^2$  for Ti blank and Ti modified with a  $C_2H_2O_4$  solution at  $60\text{ }^\circ\text{C}$  for 5 h, respectively. The electrochemical active surface areas obtained in a 0.1 M KCl solution by cyclic voltammetry following the method of Trasatti and coworkers[36], gives values of  $4.78 \times 10^{-5} \pm 1.34 \times 10^{-9}$  and  $1.78 \times 10^{-5} \pm 2.25 \times 10^{-10}\text{ cm}^2$  for the Ti blank and Ti modified with a  $C_2H_2O_4$  solution. In both methods, the similar values in the samples are attributed to the presence of impurities and defects, such as the presence of carbon on the blank Ti sample. The high percentage of carbon obtained by the EDS analysis suggests that this impurity affects the evaluation of the matrix area. Carbon is known for having not only considerable surface area and electrochemical activity but also a larger response than a metallic material. Moreover, the well-defined hexagonal crystallographic shape, such as that in the titanium sample before and after the acidic treatment in a  $C_2H_2O_4$  solution, shows a modification in its morphology and a removal of impurities but no changes in the crystallographic structure.

**Table 3.** Data showing the surface area comparison of the Ti matrix with and without modification. The electrochemical activity was determined in a 0.1 M KCl solution at room temperature.

Sample	BJH Method /m <sup>2</sup> g <sup>-1</sup>	Electrochemical activity /m <sup>2</sup>
Blank Ti	4.7* ± 1.42	4.78x10 <sup>-5</sup> ± 1.34x10 <sup>-09</sup>
Modified Ti	5.0* ± 1.56	1.78 x10 <sup>-5</sup> ± 2.25x10 <sup>-10</sup>

### 3.4. Electrochemical studies

#### 3.4.1. Electrochemical stability tests.

The formation of a passive layer is observed by long-term material exposure to the manufactured “environment” after 500 cycles of voltammetry in a 0.5 M HCl solution. Figure 5 shows the increase in capacitance as the number of cycles increase with the Ti sample without etching; the figure also shows the increase in the ohmic resistance. The above results imply the formation of a titanium surface oxide layer or any other oxide due to the EDS results, thus indicating the presence of contaminant species.

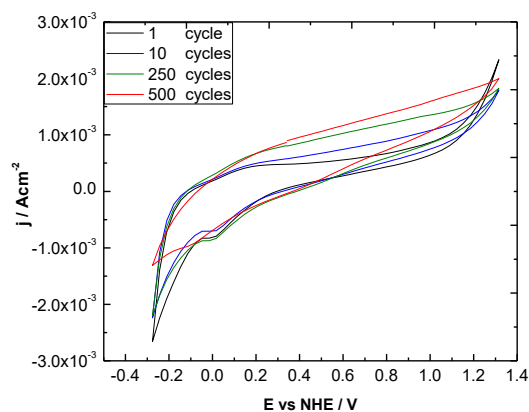


**Figure 5.** Voltammograms of the stability over time in acidic media with Ti (blank) (0.5 M H<sub>2</sub>SO<sub>4</sub> solution, 500 cycles, and  $\nu = 100 \text{ mVs}^{-1}$ ).

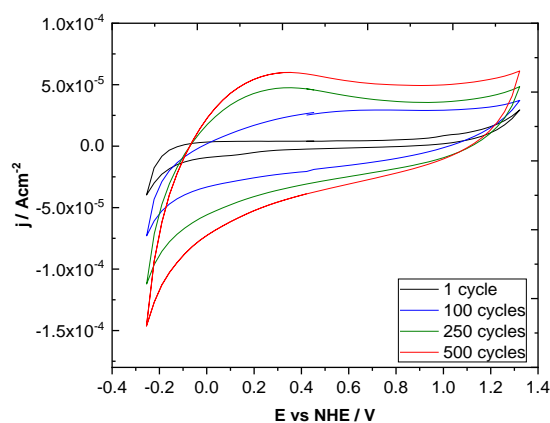


**Figure 6.** Voltammograms of the stability over time in acidic media with the Ti sample after pretreatment (0.5 M H<sub>2</sub>SO<sub>4</sub> solution, 500 cycles, and  $\nu = 100 \text{ mVs}^{-1}$ ).

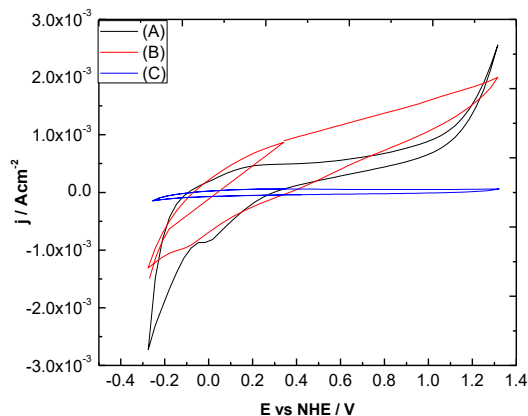


**Figure 7.** Voltammograms showing the comparison in stability between the Ti samples: blank (A), without (B) and after pretreatment (C) (0.5 M H<sub>2</sub>SO<sub>4</sub> solution, 500 cycles, and  $v = 100 \text{ mVs}^{-1}$ ).

Figure 6 illustrates the behavior through a voltammetric study. The capacitance behavior is more evident with an increasing number of cycles. After comparing both Ti samples (Figure 7), the modified sample (A) shows a better electrical connection and smaller ohmic resistance than the sample before the acidic treatment due to the effective surface modification of the oxalic acid solution [34,39–41].

### 3.4.2. Corrosion and corrosion rate

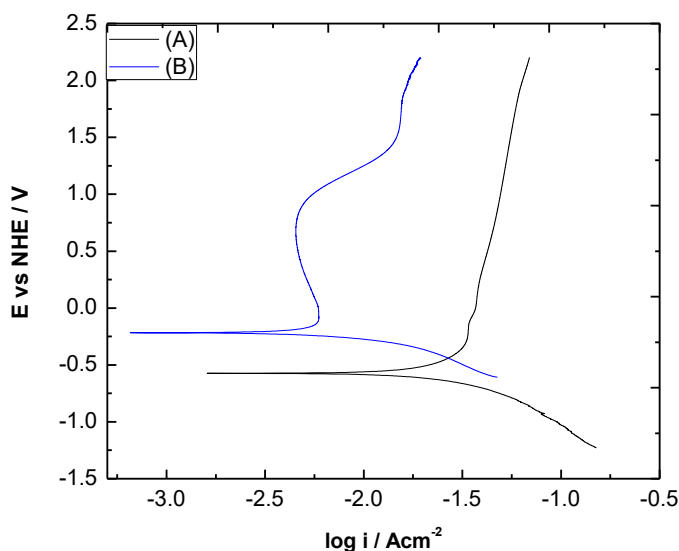


**Figure 8.** Anodic polarization curves of the Ti samples in a O<sub>2</sub>-saturated 0.5 M H<sub>2</sub>SO<sub>4</sub> solution at a 5 mVs<sup>-1</sup> scan rate and under atmospheric pressure and room temperature conditions: (A) without pretreatment and (B) after pretreatment.

The anodic polarization curves (Figure 8) show the corrosion behavior of the sample. (A) shows a long “passive” zone through corrosion, which means that a current corrosion rate exists during

the entire process [12,41]. In contrast, (B) shows that the sample has a clearly passive performance and then indicates a transpassive zone to corrosion due to a major current response; thus, it can be assumed there are more electroactive sites in the available surface area. Nevertheless, in Table 4, the corrosion potential is higher in the pretreated Ti sample compared to the blank Ti sample, with values of -0.23 and -0.57 V, respectively.

**Table 4.** Anodic polarization curve data of the Ti samples in a O<sub>2</sub>-saturated 0.5 M H<sub>2</sub>SO<sub>4</sub> solution at a 5 mVs<sup>-1</sup> scan rate and under atmospheric pressure and room temperature conditions.

Material	E <sub>corr</sub> /V	j <sub>corr</sub> /Acm <sup>-2</sup>
Blank Ti	-0.57	9.93e <sup>-5</sup>
Pretreated Ti	-0.23	1.64e <sup>-3</sup>

#### 4. CONCLUSIONS

The treatment shows a promising process to improve the GDL performance for fluid distribution but also for faster electrical conduction than a porous Ti matrix. The SEM and EDX analysis results showing small particles and high porosity with no homogeneous distribution can imply better fluid mass transport.. Moreover, this chemical process leads to better electroactive behavior along the matrix, reducing the ohmic loss and electrical distribution. An increase of 39.9% ± 0.0013 corresponding to 3766480.86 μm<sup>2</sup> can be determined from the area. Nevertheless, the above results show that this can be a preamble to subsequent modification for increased improvement.

#### ACKNOWLEDGEMENTS

The authors thank the Mexican Council for Science and Technology CONACYT for financial support through CB-2014-235848 and the projects Catedras 746, 1125. We also thank IT Cancun for the SEM image and XRD data.

#### References

1. M.V. Barros, R. Salvador, C. M. Piekarski, A. C. de Francisco, and F. M. C. S. Freire, *Int J Life Cycle Assess*, 25 (2020) 36.
2. D. K. Jonsson, B. Johansson, A. Månsson, L. J. Nilsson, M. Nilsson, and H. Sonnsjö, *Energy Strategy Reviews*, 6 (2015) 48.
3. Z. Zarhri, M.A. Aviles Cardos, Y. Ziat, M. Hammi, O. El Rhazouani, J.C. Cruz Argüello and D. Avellaneda Avellaneda, *Jallcom*, 819 (2020) 153010.
4. R. Barbosa, J. Andaverde, B. Escobar, and U. Cano, *Journal of Power Sources*, 196 (2011) 1248.
5. K.-A. Adamson, *Energy Policy*, 32 (2014) 1231.
6. G. W. Crabtree, M. S. Dresselhaus, and M. V. Buchanan, *Physics Today*, 57 (2014) 39.
7. A. C. Lloyd, *Journal of power source*, 86 (2000) 57.

8. B. Pamplona Solis, J. C. Cruz Argüello, L. Gómez Barba, M. P. Gurrola, Z. Zarhri, and D. L. TrejoArroyo, *Sustainability*, 11 (2019) 6682.
9. S. Grigoriev, V. Poremsky, and V. Fateev, *Int. J. Hydrogen Energy*, 31 (2006) 171.
10. F. Barbir, *Solar Energy*, 78 (2005) 661.
11. S. Song, H. Zhang, X. Ma, Z. Shao, R. T. Baker, and B. Yi, *Int. J. Hydrogen Energy*, 33 (2008) 4955.
12. C.-J. Tseng and S.-K. Lo, *Energy Conversion and Management*, 51 (2010) 677.
13. N. Yousfi-Steiner, Ph. Moçotéguy, D. Candusso, and D. Hissel, *Journal of Power Sources*, 194 (2009) 130.
14. G. Chen, H. Zhang, H. Zhong, and H. Ma, *Electrochimica Acta*, 55 (2010) 8801.
15. T. Ioroi, K. Yasuda, Z. Siroma, N. Fujiwara, and Y. Miyazaki, *Journal of Power Sources*, 112 (2002) 583.
16. H.-Y. Jung, S. Park, and B. N. Popov, *Journal of Power Sources*, 191 (2009) 357.
17. R. Chattot, Raphaël Chattot, O. Le Bacq, V. Beermann, S. Kühn, J. Herranz, S. Henning, L. Kühn, T. Asset, L. Guétaz, G. Renou, J. Drnec, P. Bordet, A. Pasturel, A. Eychemüller, T.J. Schmidt, P. Strasser, L. Dubau and F. Maillard, *Nature Mater*, 17 (2018) 827.
18. H.-S. Oh H.N. Nong, T. Reier, A. Bergmann, M. Gliech, J. Ferreira de Araújo, E. Willinger, R. Schlögl, D. Teschner and P. Strasser, *J. Am. Chem. Soc.*, 138 (2016) 12552.
19. D. Higgins, P. Zamani, A. Yu, and Z. Chen, *Energy Environ. Sci.*, 9 (2016) 357.
20. G. Chen, D. A. Delafuente, S. Sarangapani, and T. E. Mallouk, *Catalysis Today*, 67 (2001) 341.
21. S.-D. Yim G.G. Park, Y.J. Sohn, W.Y. Lee, Y.G. Yoon, T.H. Yang, S. Um, S.P. Yu and C.S. Kim
22. *Int. J. Hydrogen Energy*, 30 (2005) 1345.
23. T. Ioroi, T. Oku, K. Yasuda, N. Kumagai, and Y. Miyazaki, *Journal of Power Sources*, 124 (2003) 385.
24. U. Wittstadt, E. Wagner, and T. Jungmann, *Journal of Power Sources*, 145 (2005) 555.
25. C. Liu M. Carmo, G. Bender, A. Everwand, T. Lickert, J.L. Young, T. Smolinka, D. Stolten and W. Lehnert., *Electrochemistry Communications*, 97 (2018) 96.
26. S. M. M. Ehteshami, A. Taheri, and S. H. Chan, *Journal of Industrial and Engineering Chemistry*, 34 (2016) 1.
27. M. Boaro and A. S. Aricò, Eds., *Advances in Medium and High Temperature Solid Oxide Fuel Cell Technology*. Springer International Publishing, 2017, Turin, Italy
28. Y. Wang, D. Y. C. Leung, J. Xuan, and H. Wang, *Renewable and Sustainable Energy Reviews*, 65 (2016) 961.
29. E. Rasten, G. Hagen, and R. Tunold, *Electrochimica Acta*, 48 (2003) 3945.
30. T. Uchida, Y. Morikawa, H. Ikuta, M. Wakihara, and K. Suzuki, *J. Electrochem. Soc.*, 143 (1996) 2606.
31. W. Sun, B. A. Peppley, and K. Karan, *Electrochimica Acta*, 50 (2005) 3359.
32. R. Barbosa, B. Escobar, U. Cano, R. Pedicini, R. Ornelas, and E. Passalacqua, *ECS Trans.*, 41 (2011) 2061.
33. T. Jones, *Metal Finishing*, 102 (2004) 87.
34. H.-Y. Jung, S.-Y. Huang, and B. N. Popov, *Journal of Power Sources*, 195 (2010) 1950.
35. G. Tan, L. Zhou, C. Ning, Y. Tan, G. Ni, J. Liao, P. Yu, X. Chen, *Applied Surface Science*, 279 (2013) 293.
36. S. Trasatti and O. A. Petrii, *Journal of Electroanalytical Chemistry*, 327 (1992) 353.
37. I.-K. Yoon, J.-Y. Hwang, W.-C. Jang, H.-W. Kim, and U. S. Shin, *Applied Surface Science*, 301 (2014) 401.
38. S. Torquato, *Random Heterogeneous Materials: Microstructure and Macroscopic Properties*, New York: Springer-Verlag, 2002, Princeton, USA.
39. X. Zhao, J. Yao, and Y. Yi, *Transp Porous Med*, 69 (2007) 1.

40. H.-Y. Jung, S.-Y. Huang, P. Ganesan, and B. N. Popov, *Journal of Power Sources*, 194 (2009) 972.
41. Y. Li, L.X. Jiang, X.J. Lv, Y.Q. Lai, H.L. Zhang, J. Li and X. Lui, *Hydrometallurgy*, 109 (2011) 252.
42. S. Klamklang, H. Vergnes, F. Senocq, K. Pruksathorn, P. Duverneuil, and S. Damronglerd, *J Appl Electrochem*, 40 (2010) 997

© 2020 The Authors. Published by ESG ([www.electrochemsci.org](http://www.electrochemsci.org)). This article is an open access article distributed under the terms and conditions of the Creative Commons Attribution license (<http://creativecommons.org/licenses/by/4.0/>).